MANEUVERING PERFORMANCE OF A ROLLING AND PITCHING WING

C.B. Martin, F.S. Hover, and M.S. Triantafyllou
Department of Ocean Engineering
Massachusetts Institute of Technology
Cambridge, MA 02139 USA

1 Abstract

We designed and constructed an apparatus for the study of forces produced by combined roll/pitch motion of a flapping wing. The device consists of an advanced real-time data acquisition and motion control system, and a pivoting, rigid NACA0012 foil mounted to a smooth hull-like body. The maneuvering (lateral) forces created by a steady roll angle bias are found to be extremely high, with equivalent mean lift coefficients greater than three, and much higher instantaneous values.

2 Introduction

A nearly universal characteristic of biological swimmers such as cetaceans, fish, seals, and aquatic birds is the efficient generation of episodic thrust vortices for propulsion and maneuvering. This type of unsteady wake control stands in contrast to human-designed systems based on steady flow conditions in spinning propellers and over control surfaces. In general, animals far exceed the performance levels available from the traditional solutions, which has led to today's heightened interest in biomimetic designs.

Flapping wings are among the main propulsive components of most biological swimmers; they reside in the lunate tail of the tuna, in the pectoral fin of the sea-perch, and in the wing of the penguin. Understanding of the fluid mechanics of flapping wings, however, is limited by the fact that the vast majority of previous aerodynamic and hydrodynamic research has been focused on steady problems such as rigid wings at constant angles of attack. The flapping wing is an inherently unsteady problem where the instantaneous flow patterns are never the same over the course of a flapping cycle. A number of parameters are referred to throughout the literature on flapping foils:

- Free stream velocity: U
- Flapping radial frequency: ω
- Vortex-wake width: A
- Chord length: c
- Reynolds number: $Re = Uc \,/\, \nu$
- Reduced velocity: $k = \omega c \,/\, 2U$
- Strouhal number: $St = \omega A \,/\, 2\pi U$

Freymuth [3] performed experiments on a NACA 0015 airfoil in separate heaving and pitching modes, and identified the "propulsive signature" as a staggered vortex street, which forms a jet-like velocity component away from the foil. A careful examination of his figures reveals asymmetry in the vortex wake, suggesting a mean lift as would be expected with a non-zero mean angle of attack; the asymmetry is characterized by the shedding of vortices in distinct pairs that create a mushroom-shaped jet at an angle to the incoming flow. Koochesfahani [7] presented a variety of visualization and Laser Doppler Velocimetry (LDV) data for a NACA 0012 section pitching about its quarter chord point. For a sinusoidal oscillating pitch angle, the oscillating wing produces thrust above a certain reduced frequency, and the case of all vortices in line corresponds to zero thrust/drag; any staggering results in non-zero thrust/drag with a sign determined by the direction of rotation of the staggered vortices. Non-sinusoidal motions were also considered, by accelerating one half of the cycle. Typically one large vortex is shed during the fast portion of the cycle, while the slow portion of the cycle sheds multiple vortices of the same sign; this often results in three vortices shed per cycle, clearly an asymmetrical arrangement suggesting mean lift on the foil.

Gursul & Ho [4] performed experiments on a stationary two-dimensional NACA 0012 wing section held at an angle of attack to an unsteady stream. The velocity of the inflow is created in a U-tube tunnel, and described as a steady state component plus an oscillating component. The greatest mean lift coefficients generally occur at $k \approx 0.8$; the mean lift coefficient also increases with increasing (relative) velocity fluctuations. Flow visualizations suggest that mean lift is primarily a function of the amount of the cycle for which the unsteady leading edge stall vortex remains attached to the wing before shedding into the wake, and it is this behavior that is maximized at $k \approx 0.8$. The maximum mean lift coefficient shown is about 2.7, comparable with those of Read[8] (discussed below). Gursul and Ho also present phase-averaged instantaneous lift-coefficients, showing a strong peak midway through the cycle with maximum values approaching 14. It is suggested that these transient forces are a function of the intensity of the separation (leading edge) vortex as it passes the mid-chord of the wing.

Bandyopadhyay *et al.* [2] investigated the morphology of various maneuverable fish species, using video analysis to show that the maneuvering capabilities of fish which are both fast and maneuverable (mackerel and bluefish) far exceed those of man-made vehicles. Further experiments on an unsteady maneuvering device, consisting of a variable-camber dorsal fin on a cylindrical body, showed large unsteady forces which are not predicted by airfoil lifting theory.

Anderson *et al.* [1] conducted extensive experiments with heaving and pitching NACA 0012 foils for a variety of harmonic motions. A search through the motion parameter space resulted in measured propulsive efficiencies as high as 87%. Corresponding visualization showed that the high efficiency regimes correspond to synchronization of the shedding of same-sign leading edge and trailing edge vorticity resulting in a reverse Kármán street. Efficiency is thus highly dependent on the phase angle of motion between heave and pitch, which affects the synchronization of leading and trailing vorticity shedding. Read [8] and Haugsdal [5] performed experiments on a similar apparatus addressing lift and thrust forces during: harmonic propulsion, non-harmonic propulsion, harmonic maneuvering (using a pitch bias), and one-time starting maneuvers. These results are discussed in one of our companion papers [6]. While lower propulsive efficiencies are reported than by Anderson *et al.*, the primary finding pertaining to the current paper is that a steady pitch bias can create extremely large instantaneous and mean lift forces, while also producing minimal or no drag. Read's interpolated results show a maximum mean lift coefficient with zero thrust of 4.3 at 100° phase angle, 30° maximum angle of attack, and a bias angle of 24°.

The focus of this particular work is to study the fluid loading on a three-dimensional flapping wing, modeled after the penguin wing. The maneuverability of penguins is astonishing considering the fact that their bodies are largely rigid while all maneuvering forces are generated by the flapping of wings, rotation of the head and beak, and small adjustments of the tail. Such maneuverability of a rigid hull swimming in water is encouraging to engineers seeking to incrementally (or drastically) improve the maneuvering capabilities of man-made rigid-hull vehicles.

3 Design and Construction

The design and construction of our *Sea-Lion* apparatus were driven by the following objectives: to accurately measure all six forces and moments generated by the foil, as well as its position, in order to calculate propulsive efficiency, and force and moment coefficients; to servo smooth two degree-of-freedom flapping motion (roll and pitch); and to minimize free surface and non-uniform inflow effects. More than any other design component, the hull-form shown in Figure 1 best shows the general concept of a flapping wing attached to a vehicle. A streamlined submarine-like hull form was chosen as the platform to attach a flapping wing for testing. In order to minimize free surface effects and maximize the uniformity of the input flow to the foil, the apparatus is located in the vertical and horizontal center of the MIT Testing Tank facility; the resulting blockage ratio is about one percent.

The wing is located on the bottom of the hull opposite the carriage attachment mast. This placement minimizes any effect of the fixed mast on the fluid flow around the wing, as well as any vertical accelerations of fluid which would be most likely to dissipate energy through the generation of surface wave energy. The wingspan to chord ratio is similar to that of a penguin, and the length was chosen based on 2-D flapping foil experiments conducted in [8]. Note that the wing has roll as its primary degree of freedom; it also twists about the span axis, and we refer to this latter DOF as pitch. The final dimensions are listed in Table 1; the roll and pitch coordinates are shown in Figure 1.

Length	157 cm
Hull Diameter	20 cm
Wing Span	30 cm
Wing Planform Area	135 cm^2
Average Chord	5.51 cm

Table 1: Principal dimensions of the apparatus.

The factors of primary importance in the internal design are the environmental requirements of various sensors and actuators. Economical electric motors and sensors are rarely water-proof, so we employed proven rotary shaft seals, as shown in Figure 1, which necessitated waterproofing parts of the hull. The final arrangement consists of a horizontally split central hull machined from a solid Delrin cylinder. This central Delrin portion is extended at the nose and tail by transparent acrylic tubes which are further capped by a wooden nose and tail cones. The interfaces between the acrylic hulls and the central Delrin section are sealed by a double o-ring. The carriage attachment mast attaches to the top of the central Delrin section, while the wing attaches at the bottom of this section.

The two servo-motors are housed within the tubular acrylic sections, and are mounted on two aluminum angles embedded in the central hull. The top sealing plate and the rotary shaft seals of the lower central Delrin section, and the double o-ring seals between the acrylic and Delrin sections, allow the acrylic sections of the hull to remain dry and maintain suitable environmental conditions for standard servo-motors.

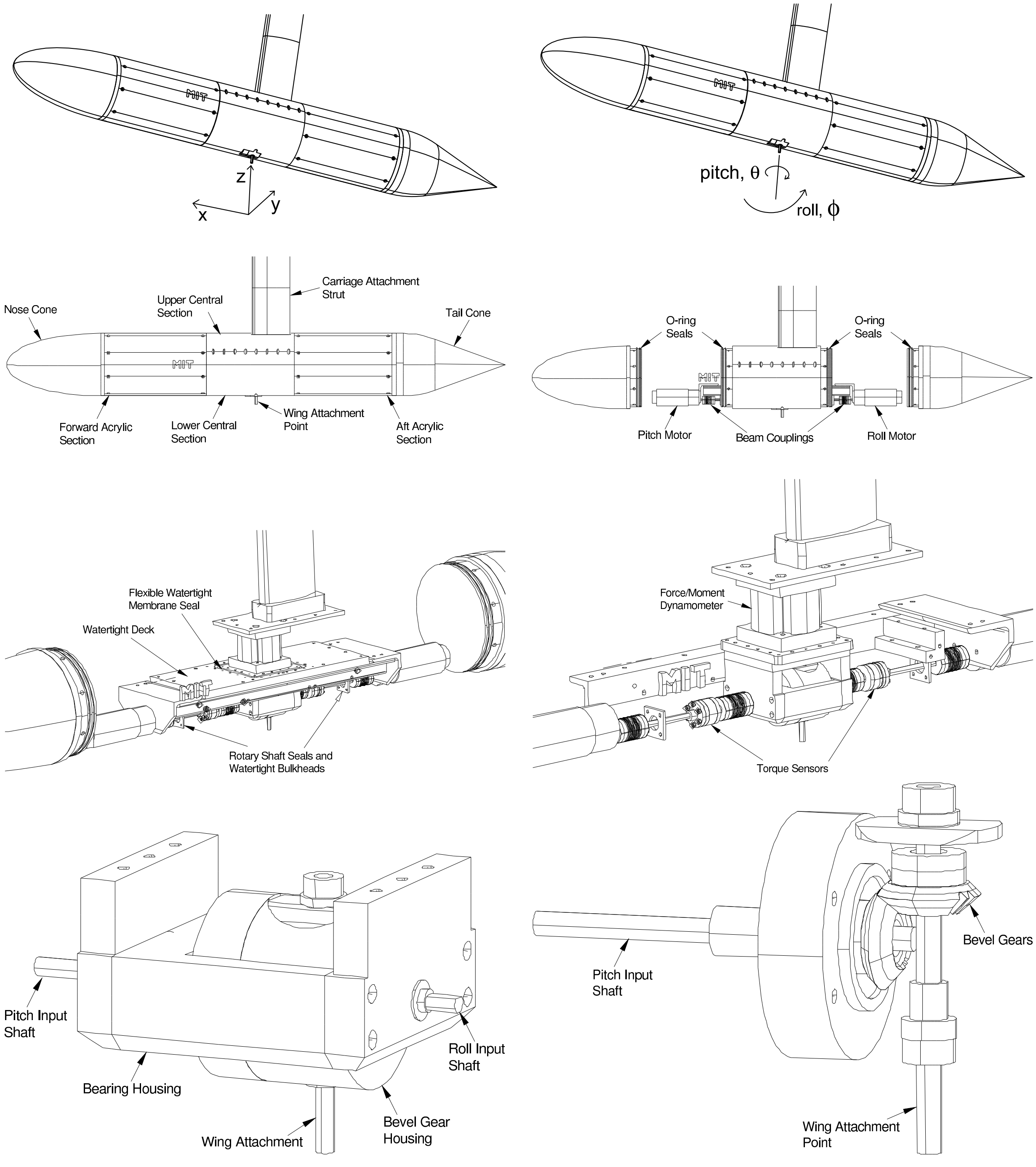

Figure 1: *From top to bottom*: Outer hull (left) and internal motor arrangement (right), vehicle coordinates, waterproofing and sensor details (showing that the motor shafts and load-cell share the loads), and flapping mechanism with bevel gear detail.

The kinematic requirements of the design are to independently control the roll and pitch positions and velocities to create the flapping-wing-like motion observed in penguins and other marine animals. In order to achieve the variety of different amplitudes, frequencies, and motion profiles, computer controlled servo-motors were chosen to drive the flapping mechanism. The main obstacles to the controllability of this flapping mechanism design are the torque capabilities of the servo-motors, mechanical backlash, transmission compliance, and proximity of feedback sensors to the objective output of the mechanism. All of these factors lead to increased error in the desired roll and pitch motion of the wing.

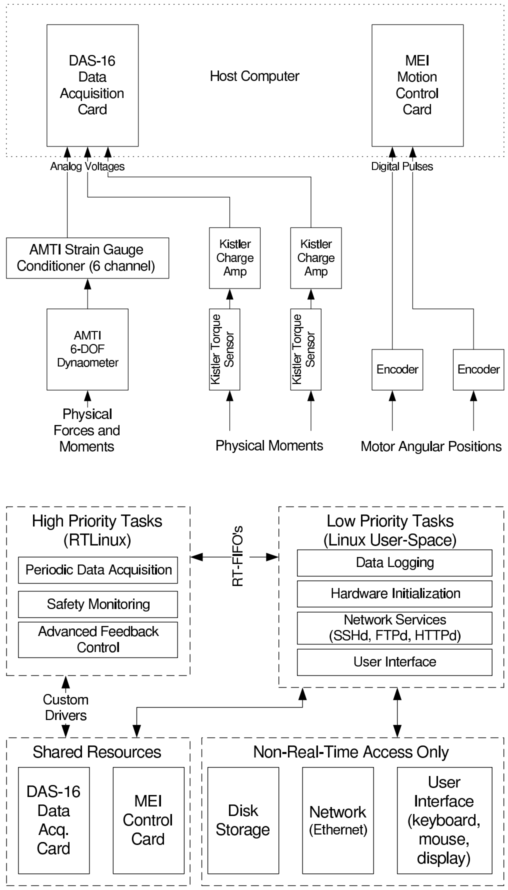

Figure 2: Data acquisition layout (top) and host computer software schematic (bottom).

The flapping mechanism uses the unique bevel-gear arrangement illustrated in Figure 1. This design allows for a direct connection from the roll control motor to the roll input of the mechanism, minimizing backlash and compliance in this primary DOF. The pitch transmission is through the bevel gear and allows the pitch control motor to be placed horizontally. The bevel-gear does introduce some backlash into the pitch transmission, and furthermore, this arrangement couples the control of the wing pitch to the roll. This coupling is a result of the fact that the bevel-gear housing actually rolls with the same angle of the wing:

$$
\begin{aligned}
\Phi(t) &= \text{roll motor position} \\
\Theta(t) &= \text{pitch motor position} \\
\phi(t) &= \text{wing roll position} \\
&= \Phi \\
\theta(t) &= \text{wing pitch position} \\
&= \Theta + \Phi
\end{aligned}
$$

The coupling of input motion to pitch angle output is accounted for by adding the commanded roll position to the desired pitch position when calculating the motion profiles for a given run. Unfortunately, this method does not account for the roll positioning error which is added to the pitch error due to the coupling.

The sensor arrangement measures all of the applied forces and moments through the use of a six-axis force/moment load-cell and two torque sensors, as illustrated in Figure 1. The load-cell is anchored to the mast attachment point, and absorbs the load carried by the main bearing housing of the flapping mechanism. The torque sensors measure the torque applied to the roll and pitch input shafts to the flapping mechanism, on the wet side of the seals. The axial and transverse forces carried by the input shafts are expected to be small, yet they do affect the overall sensitivity of the load-cell measurement. These effects are taken into account in the sensor system calibration described later. Roll and pitch position and velocity measurements are made using the servo-motor encoders.

The *Sea-Lion* software uses RTLinux (Real-Time Linux) to manage the timing of data acquisition, and to control the servos, as illustrated in Figure 2. This design requires hardware drivers to be modified for use with the Linux real-time scheduler; fortunately, source code is available for the drivers of both the data acquisition board we used and the motion control board. Only minor changes were required to allow their compilation and use with the real-time extensions. The current system is easily extensible to use custom control algorithms, including those that employ sensor feedback. While this is not yet implemented in the system, very few modifications are required to use the apparatus in a force-feedback mode, for example.

4 Sensor System Calibration

The factors complicating the *Sea-Lion* sensing system are cross-coupling and position-dependent offsets; they are handled independently and sequentially.

4.1 Position-Dependent Offset

An unfortunate consequence of the mechanical design is that minor misalignments in the flapping mechanism and external shafts and bearings result in a non-linear position-dependent offset at the load-cell output channels. This is best shown by removing the wing from the apparatus while in air and observing the load-cell measurements while rotating the motor shafts. The load-cell measurements show significant changes in force, while it is known that there is negligible change in external load with the vehicle is in air and has no wing attached.

These forces can be eliminated from the load-cell measurement by describing the offset of each of the load-cell channels as a two-parameter function of the two motor positions. Because the motors are computer-controlled, it is simple task to finely sample points on these two parameter functions, and

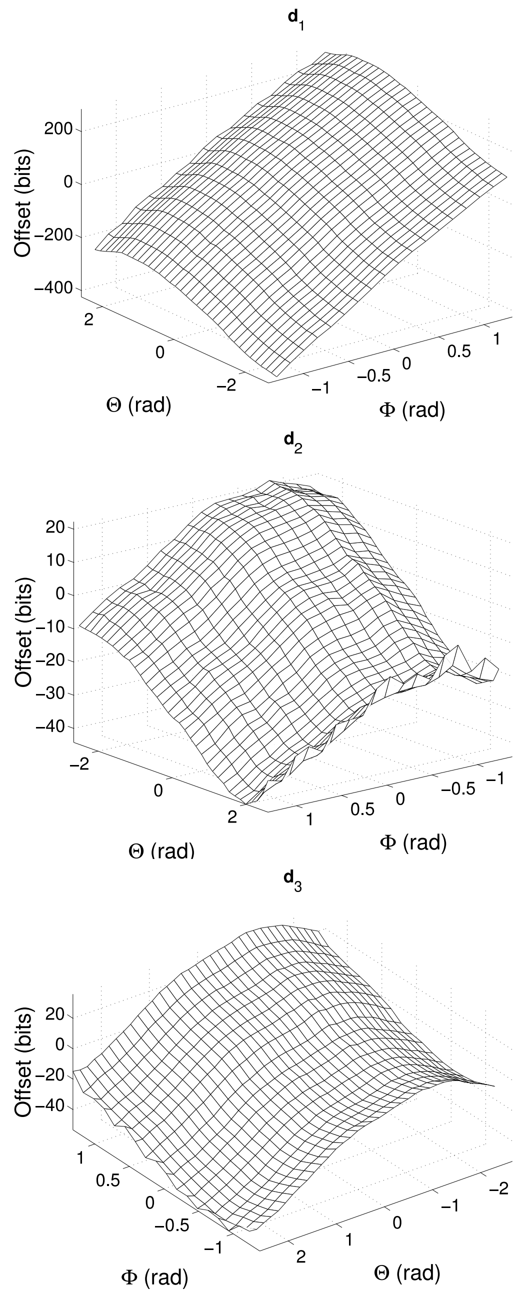

Figure 3: Position dependent offsets (only F_x, F_y, F_z shown).

later interpolate between these points to calculate corrections.

Figure 3 shows the result of a typical set of zero-load experiments for various combinations of motor positions. These samples are taken at 25 pitch motor positions for each of 25 roll motor positions. All positions are evenly incremented between the extremes of available motion. The result is the interpolation of a grid of 625 samples describing a surface that is a function of the two motor positions. Once a flapping run is completed, the recorded motor position profiles are used to calculate the offset, and subtract it, from each of the load cell channels. Then, the remaining signals are the result of external forces exclusively. Throughout our preliminary tests with the device, we did not observe significant dependency on velocity or acceleration, and concluded that only a position-dependent correction was needed.

4.2 Coupling Matrix Solution

Because the load cell is integrated into a complex structure within the hull, that attaches two motor shafts and supports the wing, it is necessary to execute a complete set of calibration tests that can identify any possible coupling between sensor measurements and applied external loads. We further make these measurements at a number of load magnitudes in order to show linearity of the coupled system. The results of these calibrations are recorded into two matrices: the matrix of known loads in each of the primary directions (modes) (L), and the matrix of measured voltages (R). The relationship between these two matrices is the calibration matrix (S):

$$\begin{aligned} RS &= L \\ S &= R\backslash L, \end{aligned}$$

where the backslash (\) operator denotes solving the over-determined linear system in the least-squares sense; the system is over-determined because tests were conducted with three sets of weights, giving much more information than is required for a unique solution. Then for any measurement vector $\vec{r}$, the load is $\vec{l}$:

$$\begin{aligned} \vec{l} &= \vec{r}S, \text{ where} \\ \vec{l} &= [F_x, F_y, F_z, M_x, M_y, M_z, M_s] \\ \vec{r} &= [d_1, d_2, d_3, d_4, d_5, d_6, \tau_1, \tau_2] \end{aligned}$$

The load vector $\vec{l}$ comprises three forces and three moments on the wing's pivot point, plus an additional load M_s. This latter is the pitch, or twist, moment carried by the pitch motor alone, and must be

	F_x	F_y	F_z	M_x	M_y	M_z	M_s
d_1	-192	-256	1533	40	-23	1	7
d_2	-136	32	25	2	-12	0	0
d_3	13	1	489	0	-9	0	0
d_4	-27	-15	43	1	9	0	0
d_5	-145	-297	1177	31	-18	0	6
d_6	-13	-72	113	2	-3	2	-1
τ_1	180	-45	-19	-15	0	0	0
τ_2	-177	-68	190	16	-7	-9	-15

Table 2: Typical calibration matrix S.

included since a pitch load on the wing is shared by the motor shaft and the load-cell, as a result of the bevel gearing. Isolation of this channel is achieved by externally fixing the bevel housing so that no twist moment reaches the load cell. The measurement vector $\vec{r}$ consists of six load cell readings and two from the shaft-mounted torque sensors. Our L-matrix for a regular calibration had twenty-four rows (three magnitudes times seven modes, plus three additional tests), and seven columns (the independent load channels). R has twenty-four rows and eight columns (eight sensors), and thus S is an 8×7 matrix.

The system is strongly coupled through the various sensor channels, as suggested by the typical S-matrix of Table 2. In particular, the existence of a dependence of the overall loads on shaft torque implies that the shafts indeed carry non-torque loads that are proportional to the torque measured by the sensor. Nonetheless, we find that the accuracy of the least squares solution is good; numbers shown in Table 3 are percent error of RS based on the maximum load applied for each principle direction for all 24 calibration runs.

#	F_x	F_y	F_z	M_x	M_y	M_z	M_s
1	0.2	-1.7	-0.4	-0.5	0.2	-0.9	-0.3
2	1.4	4.1	7.7	-0.5	-1.4	1.6	-1.5
3	0.2	-1.2	-2.1	-0.6	0.4	-1.6	-0.4
4	0.2	-1.5	0.0	-0.5	0.4	-0.9	-0.6
5	0.6	2.8	1.6	-0.5	-1.2	0.6	-0.5
6	0.1	-0.4	-1.9	0.0	0.4	-1.7	-0.0
7	-0.2	1.5	-0.3	0.4	0.2	0.2	0.6
8	-0.5	-1.7	-0.2	0.1	0.9	0.7	0.2
9	-0.6	-1.2	-0.7	0.7	-0.1	1.2	1.0
10	-1.1	-1.8	-1.6	-0.8	1.4	0.4	0.0
11	-0.1	-0.9	0.1	-0.0	0.2	0.3	0.0
12	1.0	1.5	1.4	0.2	-0.5	-0.3	-0.2
13	-1.6	-3.8	-2.8	-0.6	0.0	1.1	0.2
14	0.0	2.0	-2.2	0.5	-0.8	-0.1	0.1
15	0.3	0.0	2.0	-0.0	0.4	-0.4	-0.0
16	3.3	-2.2	1.0	0.1	0.2	0.1	-0.0
17	-0.7	-0.7	-0.4	0.3	0.6	-0.1	0.0
18	-1.0	0.6	-1.5	-0.1	-0.3	-0.3	0.2
19	0.1	-0.3	1.7	-0.8	-1.2	0.6	-0.2
20	-0.0	-0.5	-0.6	-0.4	1.4	0.6	-0.3
21	-0.2	1.0	3.3	-0.9	0.3	1.3	-0.5
22	0.2	2.9	1.9	0.6	-1.3	1.2	-0.4
23	-0.4	-2.2	-5.2	0.9	-0.0	-3.2	1.2
24	0.6	1.3	1.8	-0.4	-0.1	0.0	-0.8

Table 3: Typical Calibration: Percent Error of FS

5 Maneuvering Experiments

The towing speed for all maneuvering tests is set at 0.40 m/s, resulting in about 10 to 20 steady-state cycles measured during a run. The Reynolds number based on the average chord for all experiments is 20,000. Mean performance data is calculated as the mean over the maximum number of steady state cycles, while time-domain data is presented as phase-averaged values. In order to reduce the effects of control backlash, a high-frequency low-amplitude dither was added to the motor command position. This dither was intended to be of the same amplitude of the backlash (about 3°) in the transmission. It was found through trial and error that a dither frequency of 50Hz gave the most apparent stiffness while manually handling the wing underwater.

All experiments conducted were based on a harmonic swimming model consisting of a sinusoidal roll angle ϕ with sinusoidal wing pitch angle θ:

$$\begin{aligned} \phi(t) &= \phi_o \sin(\omega t) \\ \theta(t) &= \theta_o \sin(\omega t - \psi) \end{aligned}$$

The four non-dimensional parameters used to describe the style of flapping motion are: phase angle ψ between roll and pitch, Strouhal number based on mid-span distance r_m:

$$St = \frac{\omega \phi_o r_m}{2\pi U},$$

maximum angle of attack achieved at the mid-span $\alpha_{max,m}$, and the roll amplitude ϕ_o. The angle of attack has a nonlinear dependence on roll, frequency, and pitch as follows:

$$\alpha(t) = \theta(t) - \arctan\left[\frac{\phi_o \omega r \cos(\omega t)}{U}\right]$$

The maneuvering experiments were conducted for four unique combinations of the non-dimensional parameters. These unique combinations are referred to as "styles" because they define the harmonic flapping motion of any roll/pitch flapping system. A preliminary sampling of the parameter space was used to calculate a rough estimate of the relative propulsive efficiencies between runs. Styles #1 and #2 showed the largest efficiency based on this calculation, while Styles #3 and #4 showed very low efficiency, but relatively large side-force amplitudes. The primary kinematic differences between the first style group and the second are higher Strouhal number and lower maximum midspan angle of attack for the first pair. Within each pair, the only difference is the roll amplitude; see Table 4.

One way to create mean side forces with a harmonically flapping wing is to change the average pitch angle to a non-zero value. By flapping with a non-zero pitch angle, the resulting angle of attack

Style	#1	#2	#3	#4
ψ, rad	$\pi/2$	$\pi/2$	$\pi/2$	$\pi/2$
St	0.359	0.359	0.299	0.299
$\alpha_{max,m}$, rad	0.262	0.262	0.873	0.873
ϕ_o, rad	0.639	1.012	1.198	1.012
θ_o, rad	1.184	1.184	0.209	0.209
ω, rad/s	9.425	5.953	4.183	4.953

Table 4: Flapping Styles tested.

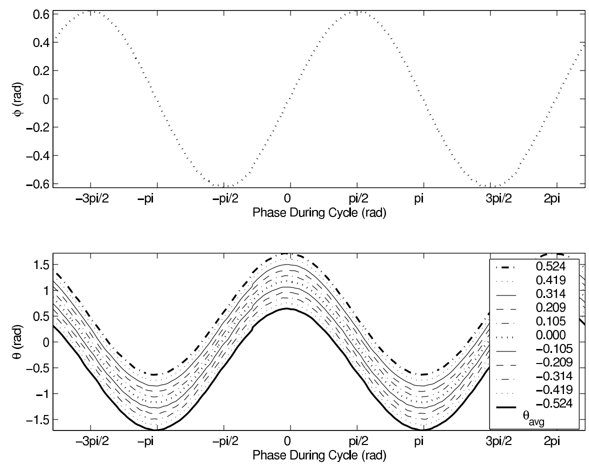

Figure 4: Kinematics at various pitch bias (Style #1).

profile will have non-zero mean, resulting in non-symmetric lift forces. This type of bias experiment was conducted for each of the styles, at eleven increments of bias angle in the range ± 0.524 rad ($\pm 30°$). Figure 4 shows the flapping kinematics for Style #1 at various pitch bias angles. The roll profile does not change for the various pitch bias angles.

A primary performance parameter for evaluating maneuvering performance is the lift coefficient C_L based on planform area, defined as:

$$C_L = \frac{F_y}{\frac{1}{2}\rho U^2 \bar{c} s}.$$

where $\bar{c}$ is the mean chord, and s is the span. Another important parameter is the power input from the motors required to generate lift forces. Power for an angular actuation system is the product of torque and angular velocity, and the average power input is the average of the power over a number of complete cycles:

$$\begin{aligned} P &= M_x \dot{\phi} + M_s \dot{\theta} \\ \bar{P} &= \frac{\int_0^{nT} P dt}{nT} \\ C_p &= \frac{\bar{P}}{\frac{1}{2}\rho U^3 \bar{c} s}. \end{aligned}$$

It is important to note that calculating the power in this way is not representative of the actual power applied to the *Sea-Lion*, which is somewhat higher. By averaging the power input over a cycle, as above, any negative power input balances a corresponding amount of positive power input, reducing the power coefficient. In applications, an actuation system would likely take advantage of the negative power portions of the cycle, by absorbing that energy and releasing it in the positive power portion of the cycle. A tuned spring system is one of many possible designs that accomplishes this.

Figure 5 shows the average results for lift coefficient and power input for all tested swimming styles and pitch bias angles. The actual values given are subject to about 3° of positioning uncertainty due to backlash. The plot of average power input lacks a clean symmetry between positive and negative pitch bias angles, for this reason.

As expected, larger pitch bias angles result in larger lift coefficients, and in the range tested, the dependence of lift on pitch bias is nearly linear for all swimming styles. The results show surprisingly large lift coefficients, particularly for Style #1. Typical zero-camber, infinite aspect-ratio wings without lift enhancement devices are capable of lift coefficients of around one before stalling. Finite aspect-ratio wings can delay stall to higher angles of attack, but generally with reduced lift slope. Styles #1 and #2 appear to be most capable of producing large lift forces, while at the same time using less motor power than the other two styles. There is a missing component of the true input power required to generate lift that is not shown in these plots, however: the thrust or drag produced by the flapping wing, which enters into any reasonable assessment of power efficiency. Unfortunately, attempts at measuring the thrust/drag force with this apparatus were unreliable, and none of the data is presented here. It would be premature to conclude that the first two styles are generally superior in average performance to the last two.

Time-domain results give insight as to the fluidic source of the forces, that is, the role of angle of attack, and also into the nature of the dynamic response as it pertains to designing a sufficiently strong, and possibly resonant, actuation structure. The results below are given as a function of "phase during a cycle" in radians. This phase is defined as zero at the up-crossing of zero in the roll motion, π at the down crossing, and 2π or zero at the following up-crossing. This allows presentation on the same axes of data that are of different frequencies.

Figure 6 shows the instantaneous lift coefficient for swimming Style #1 over the range of tested pitch bias angles; the maximum measured forces are three to four times the average forces. For the higher-lift runs, there are two lift peaks, one large and one small per cycle. With small bias, the mean lift is near zero, while the peak values still reach nearly five. The force profiles are very similar between the positive and negative pitch bias angle cases; this

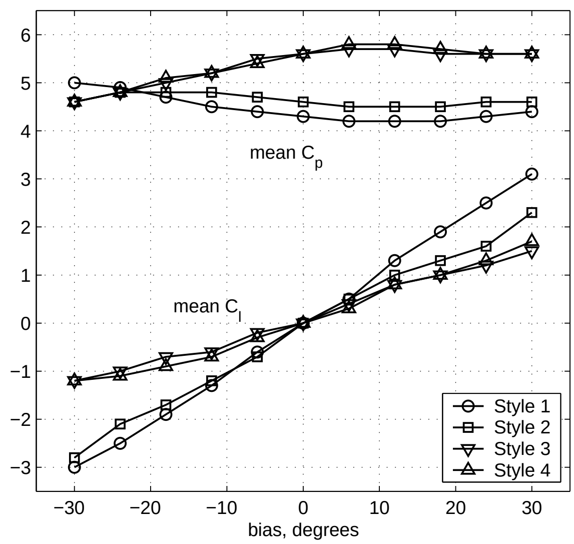

Figure 5: Mean performance results for pitch bias experiments.

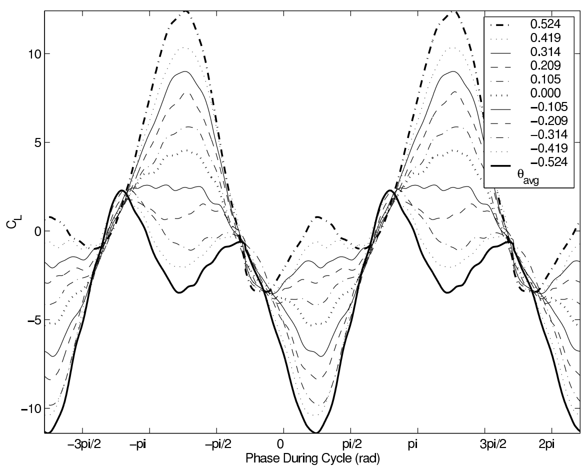

Figure 6: Lift coefficients (Style #1).

is evident by looking closely at the curves marked ±0.524. By flipping one of these profiles vertically about the zero force line and phase shifting by a half cycle, the general forms of the curves are seen to be very similar, suggesting that any effect of asymmetric position error coupling is incremental.

Figures 7 and 8 show the moments in roll and pitch generated by the foil, and indicate the torques required by any actuation system of such a device. The moments are presented in their non-dimensional coefficient form, where the normalization factor is stagnation pressure times planform area times wingspan.

$$C_M = \frac{M}{\frac{1}{2}\rho U^2 \bar{c} s^2}$$

The measured roll torques shown in Figure 7

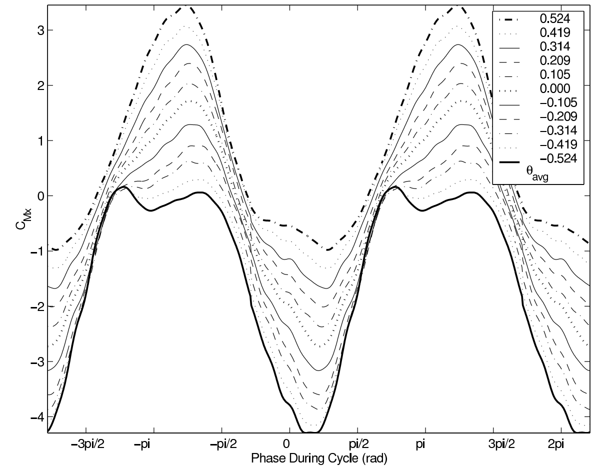

Figure 7: Roll moment coefficients M_x (Style #1).

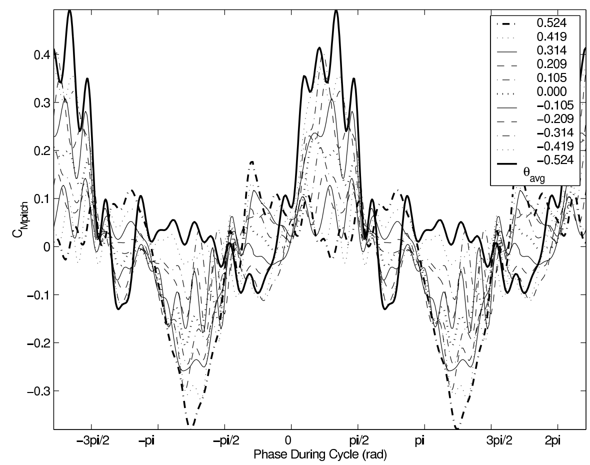

Figure 8: Pitch moment coefficients M_z (Style #1).

contain, generally, the same frequency of the flapping motion, with a smaller amplitude, higher frequency disturbance seen most clearly at the torque peaks. This is suggestive of the effects of vortex shedding, but flow visualization is required to confirm such intuitions. The pattern caused by changing the pitch bias angle in increments is striking in its regularity and apparent symmetry.

The measured pitch torques shown in Figure 8 are much less clear than the other measurements, because they are quite small. This is an important design point, that driving the pitch of the foil requires much less power than the roll. A smaller pitch motor could be used, and perhaps integrated into the current bevel gear housing, eliminating the need for bevel gears altogether. Another interesting possibility for control of the pitch of the wing would be to design a passive system that could approximate these force profiles. Clearly, such a system would be incapable of mean power input, but with such small forces and power involved, perhaps passive control would be sufficient.

6 Summary

This experimental work confirms prior studies, showing that large lift coefficients are available in flapping wings of symmetric section without lift enhancement devices such a flaps or boundary layer injection [4], [8]. We found that these large lift forces are not limited to two-dimensional sections, but can be produced by roll/pitch kinematics; average lift coefficients in excess of three are measured at a pitch bias angle of 30°.

No optimization of the swimming parameters has been completed at this time, so that applications may only become more practical with further development. In addition to the rigid-foil, harmonic motion parameters explored in this work, a number of other variations are also being explored including: span-wise distribution of chord, wing thickness profile, camber, wing flexibility (homogeneous and directional), non-harmonic motions, and force-feedback control.

The primary difficulty encountered with the *Sea-Lion* was the lack of reliability of the thrust/drag measurement, and the lack of precise control of wing pitch. Both situations could be improved for the current device by integrating the pitch motor into the bevel-gear housing, eliminating the need for the bevel-gears. This design change would require a water-proof motor, but would lessen backlash in the pitch transmission, and decouple the pitch error from the roll error.

ACKNOWLEDGEMENT: Support from the Office of Naval Research, Contract N00014-99-1-1082, monitored by Dr. Teresa McMullen and Dr. P. Bandyopadhyay, is gratefully acknowledged.

References

[1] J. M. Anderson, K. Streitlien, D. S. Barrett, and M. S. Triantafyllou. Oscillating foils of high propulsive efficiency. *Journal of Fluid Mechanics*, 360:41–72, 1998.

[2] P. R. Bandyopadhyay, J. M. Castano, J. Q. Rice, R. B. Phillips, W. H. Nedderman, and W. K. Macy. Low-speed maneuvering hydrodynamics of fish and small underwater vehicles. *Journal of Fluids Engineering*, 119:136–144, 1997.

[3] P. Freymuth. Propulsive vortical signature of plunging and pitching airfoils. *AIAA Journal*, 26(7):881–882, July 1988.

[4] I. Gursul and C.-M. Ho. High aerodynamic loads on an airfoil submerged in an unsteady stream. *AIAA Journal*, 30(4):1117–1119, April 1992.

[5] Ø. Haugsdal. Motion control of oscillating foils for steady propulsion and starting maneuvers. Master's project, NTNU, Department of Marine Technology, December 2000.

[6] F.S. Hover, D.A. Read, , and M.S. Triantafyllou. Experiments with a 2-d oscillating foil for propulsion and maneuvering. In *Proc. UUST*, Durham, NH, 2001.

[7] M. M. Koochesfahani. Vortical patterns in the wake of an oscillating airfoil. *AIAA Journal*, 27(9):1200–1205, September 1989.

[8] D. A. Read. Oscillating foils for propulsion and maneuvering of ships and underwater vehicles. Master's project, Massachusets Institute of Technology, Department of Ocean Engineering, February 2000.